Legends for Supplementary Figures:

Suppl. Fig. 1. Palmitoylation level of CL3 regulates its targeting to dendritic rafts.

(A) Visualization of raft-targeted GFP-CL3 in hippocampal neurons. A fraction of GFP-CL3 was resistant to Triton X-100 extraction at the perinuclear region and in the dendrites (arrowhead and arrow, -GODZ). A fluorescence linescan traversing orthogonal to the dendrite (at the arrow position) reveals the presence of significant cluster of fluorescence (-GODZ; see inset for fluorescence profile). Co-expression of GODZ with GFP-CL3 enhanced accumulation of GFP-CL3 into detergent-resistant membrane patches at the perinuclear Golgi apparatus and dendrites (arrowheads, +GODZ), as shown by more prominent peak amplitudes in the fluorescence profile (scanned at the arrow, inset). Coexpressed mRFP signal was undetected in these permeabilized neurons indicating that cytosolic proteins were thoroughly washed out. Thus, CL3 palmitoylation regulated targeting of CL3 into dendritic rafts.

(B) Representative images of detergent-solubilized hippocampal neurons transfected with GFP-CL3 and MAP2-CTF-RFP. Detergent-resistant GFP-CL3 patches are detected in MAP2-positive dendritic processes. Examplar cases are shown as 2 rectangular regions of interest along the MAP2-positive dendritic segments. Scale bars, 10 μm (A and B); 2 μm (inset in [A]).

Suppl. Fig. 2. Properties of dendritic raft-targeted CL3.

(A) CL3 forms a multimeric complex in living hippocampal neurons. A significant intermolecular FRET was revealed between CFP-CL3 and YFP-CL3, but not between CFP-CL3 and YFP. YFP-CL3/CFP-CL3, 6.76 ± 1.22 ($n = 9$); YFP/CFP-CL3, 0.09 ± 0.4 ($n = 8$); **, $p < 0.01$ (*t*-test).

(B) CFP-CL3 co-localized with dendritic puncta of Lyn-YFP, a signaling molecule highly

enriched in lipid rafts, in untreated neurons. However, detergent extraction in live neurons revealed that raft-inserted CFP-CL3 and Lyn-YFP were actually present on distinct rafts.

(C) In contrast, there was a partial overlap between the dendritic punctate distribution of detergent-resistant EGFP-GluR1 and that of mCherry-CL3 (arrowheads).

Scale bar, 10 μm.

Suppl. Fig. 3. Cumulative probability analysis of primary dendrites in CL3-knockdown neurons.

CL3 knockdown showed a prominent reduction in primary dendrite size throughout the range of dendrite length observed. Numbers of examined dendrites (number of neurons): shNega, n = 158 (from 34 neurons); shCL3, n = 133 (from 33 neurons). ***, $p<0.001$ (Kolmogorov-Smirnov test).

Suppl. Fig. 4. Dendritic but not axonal formation is severely affected even when initial plating occurred following an extensive CL3-knockdown period in a suspension culture of cortical neurons.

(A) Diagram of experimental procedure. A suspension culture of electroporated neurons was maintained for 48 h and then plated following mechanical re-dissociation. This second dissociation step completely severed all processes formed in the aggregates in solution. Twenty-four hours later, an axon and several dendrites (arrowheads and arrows, respectively) were formed and subjected to morphometrical analysis.

(B, C). CL3 knockdown caused a strong suppression of dendritic length and tip number, but the effect on axon formation was negligible and not significant. Wildtype CL3, but neither a palmitoylation sites-deficient mutant 4CS, nor a prenylation site-mutant C474S (which is also

unable to be palmitoylated, see Fig. 1) was able to rescue the specific impairment in dendrite outgrowth, suggesting a critical role for accurate sequential lipidification of CL3 during dendrite growth. Number of neurons: shNega + Mock, n = 15; shCL3 + Mock, n = 15; shCL3 + WTres, n = 15, shCL3 + 4CSres, n = 15, shCL3 + C474Sres, n = 15. *, $p<0.05$; ***, $p<0.001$; n.s., $p>0.05$ (ANOVA with posthoc Tukey-Kramer test). Scale bar, 100 μm.

Suppl. Fig. 5. Early dendritogenesis is not affected by knockdown of either CaMKIIα or CaMKIV, two CaMK species previously shown to be involved in dendritic maturation.
Number of neurons: shNega, n = 15; shCL3, n = 15; shCaMKIIα, n = 15; shCaMKIV, n = 15. ***, $p<0.001$ (ANOVA with posthoc Tukey-Kramer test).

Suppl. Fig. 6. Disruption of dendrite morphology in mature hippocampal neurons by CL3-knockdown.
(A) Hippocampal neurons were transfected with shRNA vectors at 7 DIV and observed at 9 DIV. A representative image of hippocampal neuron expressing either shNega or shCL3 vector is shown. Scale bar, 50 μm.
(B) Quantification of dendritic arborization on hippocampal neurons. Only primary dendrites were traced. Dendritic arborization was severely disrupted in shCL3-neuron, as quantified by measurement of either total length or tip number of primary dendrites. Co-expression of an shCL3-resistant CL3 wildtype rescued this effect, strongly supporting the idea that CL3 may be also involved in determining dendrite morphology after synaptogenesis. Number of neurons: shNega + Mock, n = 13; shCL3 + Mock, n = 18; shCL3 + WTres, n = 18.
*, $p<0.05$; **, $p<0.01$ (ANOVA with posthoc Tukey-Kramer test).

Suppl. Fig. 7. Deformation of Golgi apparatus in CL3-knockdown hippocampal neurons.

(A) Hippocampal neurons were transfected with shCL3 vectors at 7 DIV and analyzed at 9 DIV. The Golgi morphology was visualized by GM130 immunostaining. An aberrant, disassembled pattern of Golgi distribution with an increased number of smaller patches was observed by CL3-knockdown (arrows). Scale bar, 10 μm.

(B) Quantification of Golgi area and number of Golgi membrane fragments (see Supplementary Experimental Procedures for definition). CL3 knockdown did not affect Golgi area defined as total GM130-positive area, while it induced significant disorganization of Golgi membrane structures that was reminiscent of Golgi vesiculation. Number of examined neurons: shNega, n = 10; shCL3, n = 10. *, $p<0.05$; n.s., not significant (*t*-test).

Suppl. Fig. 8. Inaccessibility of 4CS mutant CL3 to detergent-resistant raft membranes in CL3-knockdown cells.

(A) Quantification of raft-targeted CL3. Increased palmitoylation (+GODZ) significantly augmented the amount of Triton X-100-resistant pool of CL3. Overexpression of a palmitoylation-deficient CL3 (4CS) alone did not reveal a marked change compared to wildtype. In contrast, however, GFP signal of $4CS_{res}$ mutant was lost and undistinguishable from background (n.d., not detectable) in detergent-extracted neurons in which endogenous CL3 was knockdowned, even though comparable level of expression of WT and 4CS was visually verified prior to Triton X-100 treatment. This indicated that in principle, loss of palmitoylation events rendered CL3 inaccessible to detergent-resistant dendritic rafts. However, if *endogenous* (palmitoylated) WT persisted, this might recruit a portion of an *exogenous* (non-palmitoylated) 4CS mutant to lipid rafts, presumably because of a reduced

yet non-null binding affinity between WT and a 4CS mutant.

(B) Removal of palmitoylation-defective $4CS_{res}$ mutant from rafts in a CL3 knockdown background (shCL3+$4CS_{res,}$ -GODZ) was accompanied with an aberrant formation of thin protrusions (arrows) from the soma. In contrast, this phenotype could be barely seen in a wildtype background (4CS, -GODZ). Consistent with the participation of an endogenous CL3 palmitoylation in 4CS localization, GODZ expression increased Golgi accumulation of 4CS (4CS, +GODZ). However, GODZ expression had no effect in a CL3 knockdown background (shCL3+$4CS_{res,}$ +GODZ), and did not prevent appearance of aberrant protrusions (arrows). Scale bar, 10 μm.

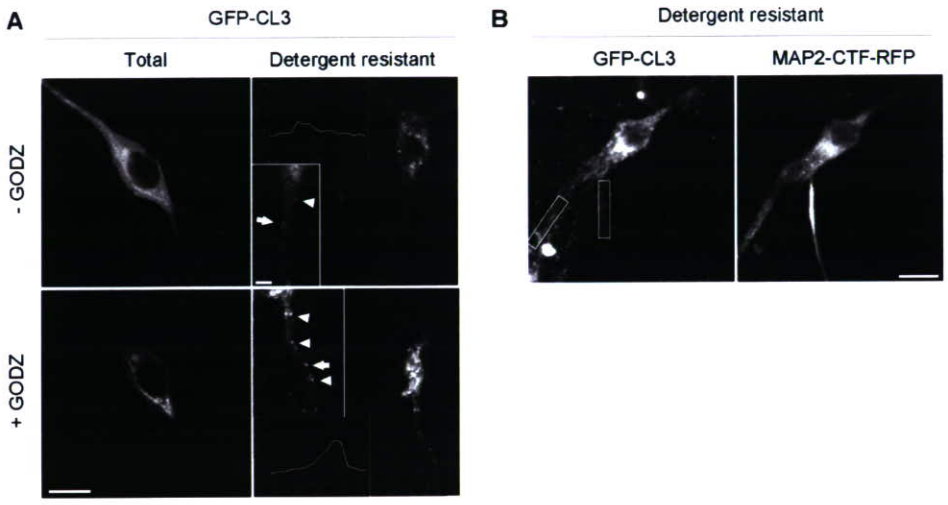
A
GFP-CL3
Total
Detergent resistant
- GODZ
+ GODZ
B
Detergent resistant
GFP-CL3
MAP2-CTF-RFP

Suppl. Fig. 1

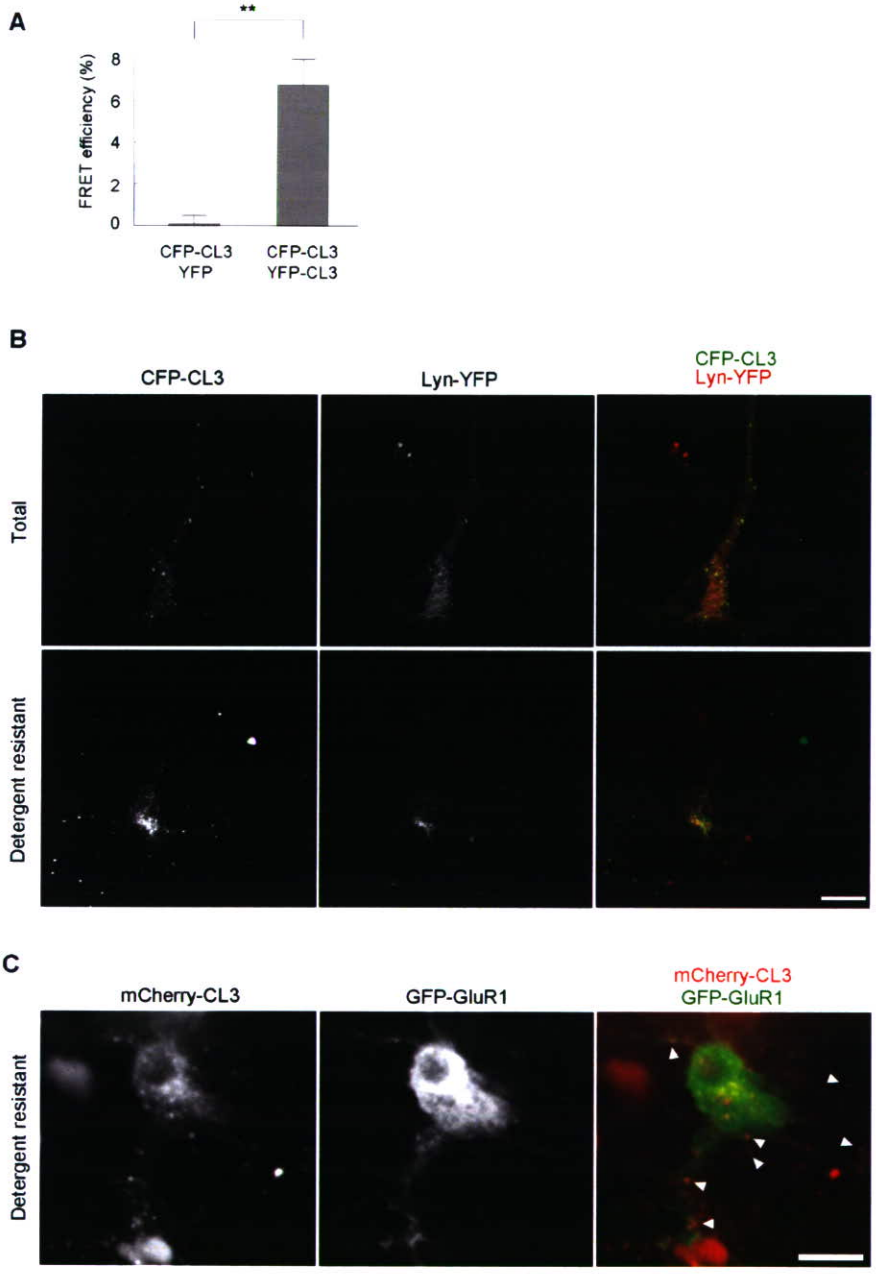
A
**
FRET efficiency (%)
8
6
4
2
0
CFP-CL3
YFP
CFP-CL3
YFP-CL3
B
CFP-CL3
Lyn-YFP
CFP-CL3
Lyn-YFP
Total
Detergent resistant
C
mCherry-CL3
GFP-GluR1
mCherry-CL3
GFP-GluR1
Detergent resistant

Suppl. Fig. 2

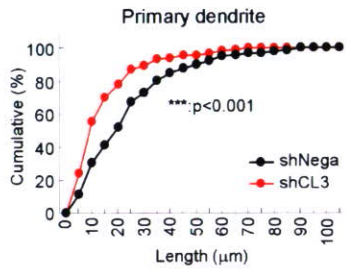
Primary dendrite
Cumulative (%)
100
80
60
40
20
0
***:p<0.001
shNega
shCL3
0
10
20
30
40
50
60
70
80
90
100
Length (μm)

Suppl. Fig. 3

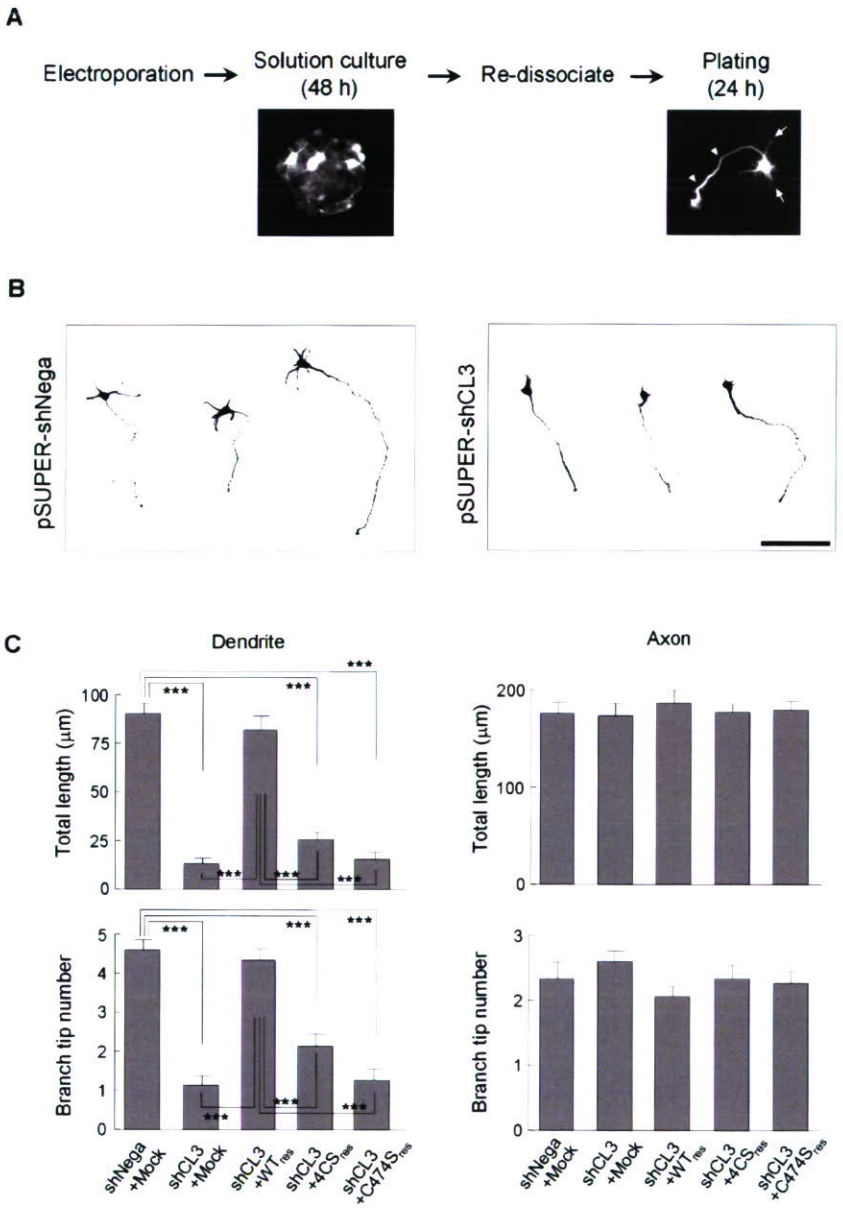
A
Electroporation
Solution culture
(48 h)
Re-dissociate
Plating
(24 h)
B
pSUPER-shNega
pSUPER-shCL3
C
Dendrite
Axon
Total length (μm)
Branch tip number
shNega +Mock
shCL3 +Mock
shCL3 +WTres
shCL3 +4CSres
shCL3 +C474Sres

Suppl. Fig. 4

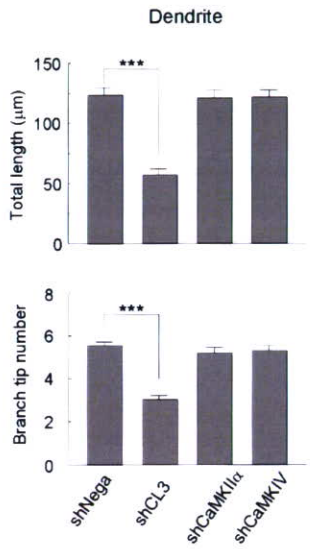
Dendrite
Total length (μm)
150
100
50
0
***
Branch tip number
8
6
4
2
0
***
shNega
shCL3
shCaMKIIα
shCaMKIV

Suppl. Fig. 5

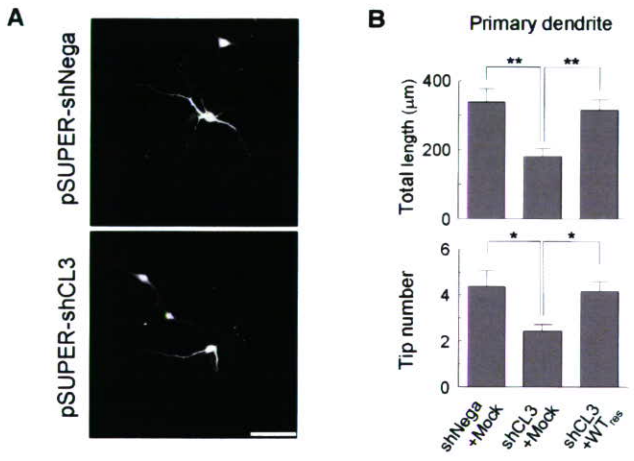
A
pSUPER-shNega
pSUPER-shCL3
B
Primary dendrite
Total length (μm)
400
200
0
**
**
Tip number
6
4
2
0
*
*
shNega +Mock
shCL3 +Mock
shCL3 +WT res

Suppl. Fig. 6

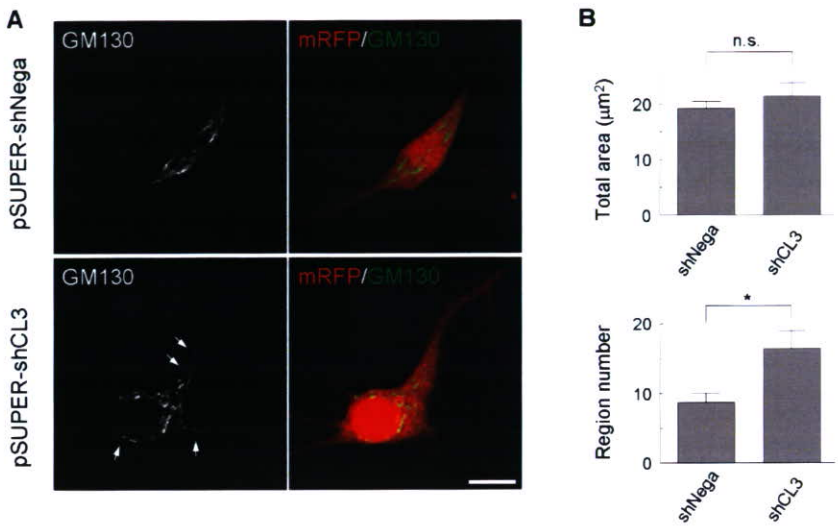
A
GM130
mRFP/GM130
pSUPER-shNega
GM130
mRFP/GM130
pSUPER-shCL3
B
n.s.
Total area (μm²)
20
10
0
shNega
shCL3
*
Region number
20
10
0
shNega
shCL3

Suppl. Fig. 7

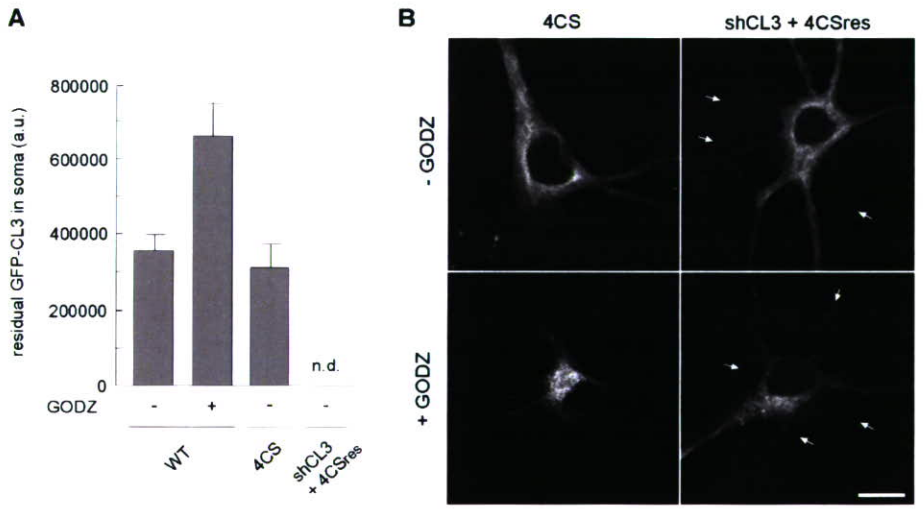
A
residual GFP-CL3 in soma (a.u.)
800000
600000
400000
200000
0
n.d.
GODZ
-
+
-
-
WT
4CS
shCL3 + 4CSres
B
4CS
shCL3 + 4CSres
- GODZ
+ GODZ

Suppl. Fig. 8

nature neuroscience

ARTICLES

© 2007 Nature Publishing Group http://www.nature.com/natureneuroscience

RIM1 confers sustained activity and neurotransmitter vesicle anchoring to presynaptic Ca^{2+} channels

Shigeki Kiyonaka[1], Minoru Wakamori[1], Takafumi Miki[1], Yoshitsugu Uriu[1], Mio Nonaka[2], Haruhiko Bito[2], Aaron M Beedle[3], Emiko Mori[1], Yuji Hara[1,3], Michel De Waard[4], Motoi Kanagawa[3], Makoto Itakura[5], Masami Takahashi[5], Kevin P Campbell[3] & Yasuo Mori[1]

The molecular organization of presynaptic active zones is important for the neurotransmitter release that is triggered by depolarization-induced Ca^{2+} influx. Here, we demonstrate a previously unknown interaction between two components of the presynaptic active zone, RIM1 and voltage-dependent Ca^{2+} channels (VDCCs), that controls neurotransmitter release in mammalian neurons. RIM1 associated with VDCC β-subunits via its C terminus to markedly suppress voltage-dependent inactivation among different neuronal VDCCs. Consistently, in pheochromocytoma neuroendocrine PC12 cells, acetylcholine release was significantly potentiated by the full-length and C-terminal RIM1 constructs, but membrane docking of vesicles was enhanced only by the full-length RIM1. The β construct beta-AID dominant negative, which disrupts the RIM1-β association, accelerated the inactivation of native VDCC currents, suppressed vesicle docking and acetylcholine release in PC12 cells, and inhibited glutamate release in cultured cerebellar neurons. Thus, RIM1 association with β in the presynaptic active zone supports release via two distinct mechanisms: sustaining Ca^{2+} influx through inhibition of channel inactivation, and anchoring neurotransmitter-containing vesicles in the vicinity of VDCCs.

The presynaptic active zone is the specific site for impulse-evoked exocytosis of neurotransmitters at synapses of the nervous system in a wide variety of species[1,2]. Fine regulation of presynaptic active zone neurotransmitter release is integral to nervous system adaptive functions, including learning, memory and cognition. The molecular organization of presynaptic active zones, where synaptic vesicles are docked in close vicinity to VDCCs at the presynaptic membrane, is essential for controlling the neurotransmitter release triggered by depolarization-induced Ca^{2+} influx. The spacing between VDCCs and vesicles influences the dynamic properties of synaptic transmission[3]. However, the molecular determinants that maintain vesicles and VDCCs within a physiologically appropriate distance have remained elusive.

Originally identified as a putative effector for the synaptic vesicle protein Rab3 (ref. 4), RIM1 is part of the RIM superfamily, whose members share a common C_2B domain at their C termini[5]. RIM1 interacts with other presynaptic active zone protein components, including Munc13, ELKS (also known as CAST), RIM-BP and liprins, to form a protein scaffold in the presynaptic nerve terminal[6–10]. Mouse knockouts showed that, in different types of synapses, RIM1 is essential for different forms of synaptic plasticity[9,11]. In the CA1-region Schaffer-collateral excitatory synapses and GABAergic synapses, RIM1 maintains normal neurotransmitter release and short-term synaptic plasticity. In excitatory CA3-region mossy fiber synapses and cerebellar parallel fiber synapses, RIM1 is necessary for presynaptic long-term synaptic plasticity. In autapses, the RIM1 deletion significantly reduces the readily releasable pool of vesicles, and it alters short-term plasticity and the properties of evoked asynchronous release[12]. However, in spite of this progress in understanding RIM1 functions, the mechanisms by which RIM1 acts remain unknown. Moreover, the physiological functions of other RIM isoforms (RIM2, RIM3 and RIM4)[5] remain unclear.

Multiple types of VDCCs that are distinguished on the basis of biophysical and pharmacological properties coexist in neurons[13]. High voltage–activated types of VDCCs that are essential for neurotransmitter release include N-, P/Q-, R- and L-types[14–16]. VDCCs are heteromultimeric protein complexes composed of the pore-forming α_1, designated as Ca_v, and auxiliary subunits α_2/δ, β and γ[17]. The α_1 subunit is encoded by ten distinct genes, whose correspondence with functional types is largely elucidated[13,17]. VDCC complexes are associated, primarily via interactions with the α_1 subunit[18–25], with presynaptic and postsynaptic proteins including syntaxin, SNAP-25, synaptotagmin, CASK and Mint. The α_1 and β subunits interact to enhance functional channel trafficking to the plasma membrane[26,27]

[1]Department of Synthetic Chemistry and Biological Chemistry, Graduate School of Engineering, Kyoto University, Katsura Campus, Nishikyo-ku, Kyoto 615-8510, Japan. [2]Department of Neurochemistry, University of Tokyo Graduate School of Medicine, Hongo 7-3-1, Bunkyo-ku, Tokyo 113-0033, Japan. [3]Howard Hughes Medical Institute and Departments of Physiology and Biophysics, Internal Medicine, and Neurology, University of Iowa Roy J. and Lucille A. Carver College of Medicine, 285 Newton Road, Iowa City, Iowa 52242-1101, USA. [4]Inserm U607, Laboratoire Canaux Calciques, Fonctions et Pathologies, 17 Rue des Martyrs, Bâtiment C3, 38054 Grenoble Cedex 09, France. [5]Department of Biochemistry, Kitasato University School of Medicine, Kitasato 1-15-1, Sagamihara, Kanagawa 228-8555, Japan. Correspondence should be addressed to Y.M. (mori@sbchem.kyoto-u.ac.jp).

Received 23 February; accepted 2 April; published online 13 May 2007; doi:10.1038/nn1904

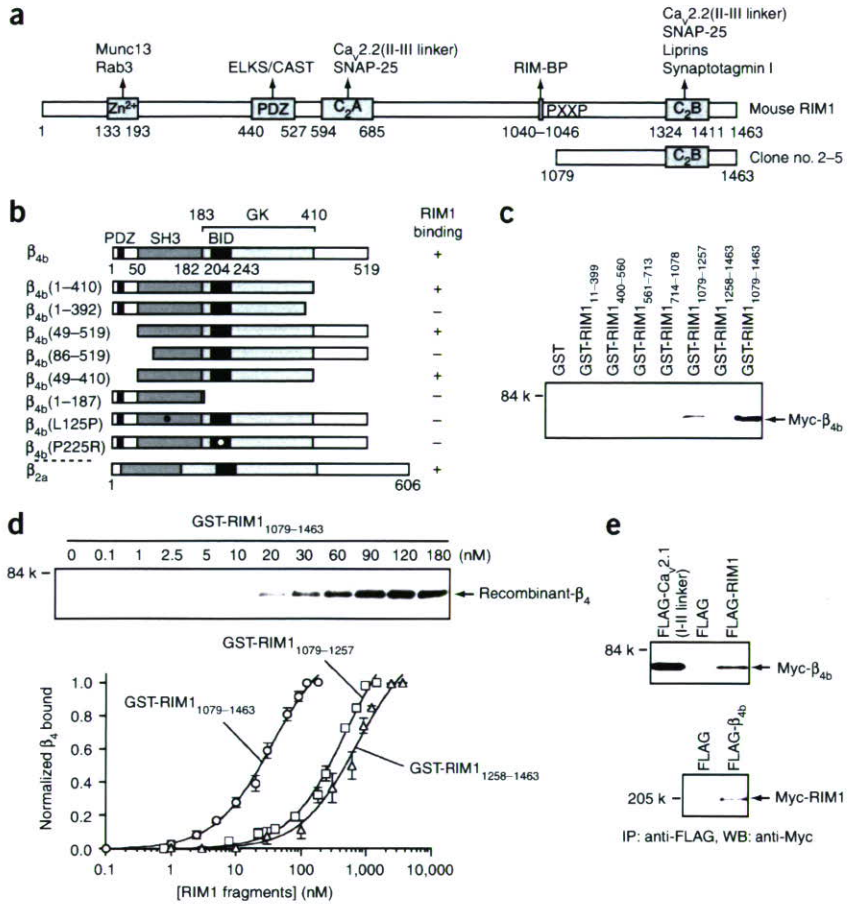

Figure 1 Direct interaction of RIM1 with the VDCC β_{4b} subunit. (**a**) Domain structure of mouse RIM1. Arrows indicate molecules interacting with RIM1 at the Zn^{2+}-finger–like domain (Zn^{2+}), PDZ domain (PDZ), first and second C_2 domains (C_2A and C_2B) and proline-rich region (PXXP)[4,6–10]. The protein region encoded by clone no. 2–5 is also indicated. (**b**) Mapping of RIM1-binding sites on β_{4b} by the yeast two-hybrid assay. β-subunit constructs in bait vectors were tested with RIM1 in the prey vector. The interactions were scored by β-galactosidase activity and His^+ prototrophy. (**c**) Pulldown assay of β_{4b} with GST fusion RIM1 mutants. GST fusion proteins immobilized on glutathione-Sepharose beads were incubated with cell lysates obtained from Myc-β_{4b}–transfected HEK293 cells. Bound proteins were analyzed by western blotting (WB) using antibody for Myc. (**d**) *In vitro* association between the purified GST-RIM1 fusion constructs and recombinant β_4 subunit (residues 47–475). GST-RIM1 proteins at various concentrations, incubated with β_4 (50 pM), were captured by glutathione-Sepharose beads. Captured β_4 proteins were examined by WB. The bottom panel shows the quantitative densitometric analysis of bands shown in the upper panel and in **Supplementary Figure 2**. The saturation curves were subjected to the nonlinear least-squares curve-fitting method to evaluate the apparent dissociation constant (K_d). k, kDa. (**e**) Interaction of recombinant β_{4b} and RIM1 in HEK293 cells. The interaction is evaluated by immunoprecipitation (IP) with antibody for FLAG, followed by WB with antibody for Myc. Top, physical association of Myc-β_{4b} with FLAG-RIM1 in comparison with a positive control FLAG-Ca$_v$2.1(I-II linker). Bottom, physical association of FLAG-β_{4b} with Myc-RIM1.

and to modify multiple kinetic properties[28]; the β subunit also interacts with other proteins[29–31]. Therefore, it is intriguing to investigate whether β subunits are involved in targeting VDCC complexes to specific subcellular machinery at presynaptic active zones for neurotransmitter release through as yet unidentified interactions. Here, we demonstrate a previously unknown molecular interaction between RIM1 and VDCC β subunits, both of which are essential presynaptic active zone proteins. The RIM1-β interaction supports the function of RIM1 in neurotransmitter release via two distinct mechanisms: the anchoring of neurotransmitter-containing vesicles in the vicinity of VDCCs, and the sustenance of Ca^{2+} influx through the inhibition of voltage-dependent inactivation.

RESULTS

VDCC β subunits directly interact with RIM1

To identify β subunit–interacting proteins that regulate presynaptic active zone organization, we performed yeast two-hybrid screening with a mouse brain complementary DNA library using the full-length rat β_{4b} subunit as a bait. The β_4 subunit was chosen because spontaneous β_4 mutant *Cacnb4*^{lh} (lethargic) mice[32] have clear neurological defects suggesting that β_4-containing VDCCs are physiologically significant in the brain. Screening identified a clone (no. 2-5) encoding the C-terminal region (residues 1079–1463) of the mouse RIM1 protein[4] including the C_2B domain (**Fig. 1a**). Subsequent two-hybrid assays using β_{4b} mutants showed that residues 49–410, containing major structural motifs such as the Src homology 3 (SH3) domain, the α_1-interacting domain known as BID and the guanylate kinase (GK) domain, were required for the interaction of β_{4b} with the RIM1 C terminus (**Fig. 1b**). β_{2a} also showed RIM1 interaction. *In vitro* pulldown assays using glutathione-*S*-transferase (GST) fusion constructs identified the RIM1 C terminus (residues 1079–1463) as a major β_4-interaction domain likely formed in concert by two adjacent subdomains (1079–1257 and 1258–1463; **Fig. 1c** and **Supplementary Fig. 1** online). An *in vitro* binding assay using purified β_4 and RIM1 recombinants revealed a dissociation constant (K_d) of 35.1 nM for $RIM1_{1079–1463}$, which was substantially lower than those of $RIM1_{1079–1257}$ (481 nM) and $RIM1_{1258–1463}$ (717 nM) (**Fig. 1d** and **Supplementary Fig. 2** online). These results, as well as the successful coimmunoprecipitation of full-length RIM1 with β_{4b} (**Fig. 1e**), suggest that a direct protein-protein interaction occurs between RIM1 and β_4.

RIM1 physically associates with native VDCCs in the brain

We characterized the association between native VDCCs and RIM1 biochemically using VDCC complexes enriched from mouse brains through microsome preparation, KCl wash, solubilization, heparin purification and sucrose density gradient fractionation[25]. Western blot analysis of sucrose gradient fractions showed cosedimentation of RIM1 with $Ca_v2.1$ and β_4 (**Fig. 2a**). Statistical analysis of cosedimentation data revealed a complete overlap of $Ca_v2.1$ and β_4, confirming that they associate in the VDCC complex (**Fig. 2b**). RIM1 sedimented in overlapping minor and major peaks: the latter completely overlapped with VDCC subunits, whereas the former did not cosediment with VDCC and is likely to represent a subset of RIM1 in a smaller,

© 2007 Nature Publishing Group http://www.nature.com/natureneuroscience

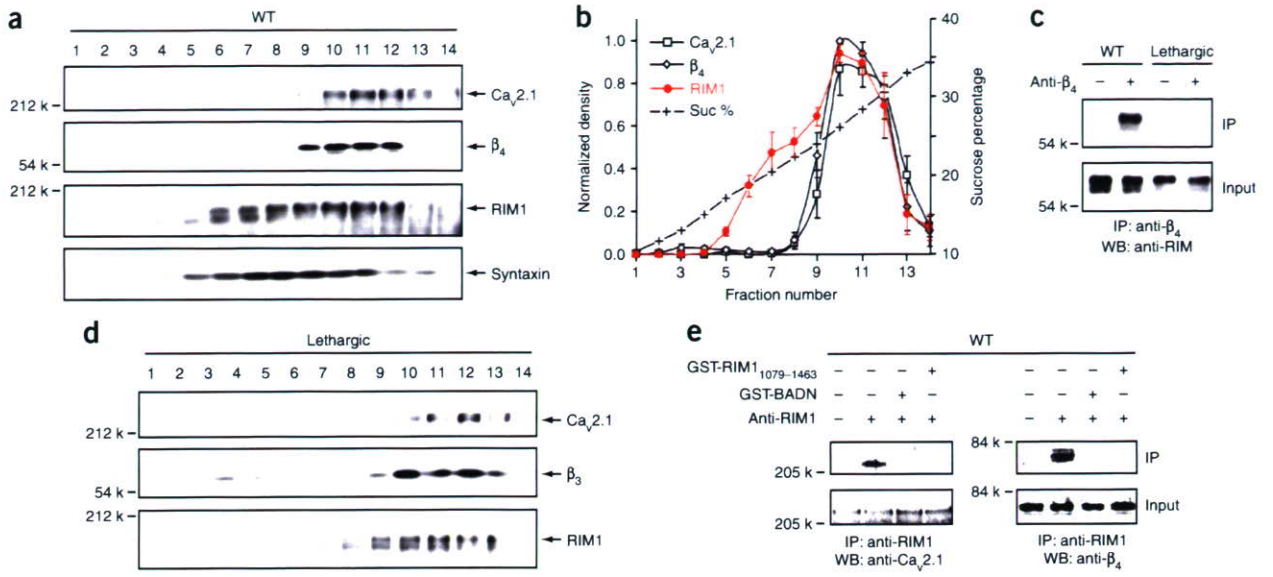

Figure 2 Association of RIM1 with native neuronal VDCC complexes. (**a**) Sucrose gradient fractionation of neuronal VDCC complexes from wild-type (WT) mouse brains and subsequent western blot (WB) showed cosedimentation of RIM1 with $Ca_v2.1$ and β_4. Syntaxin showed similar cosedimentation with RIM1. (**b**) Densitometry of $Ca_v2.1$, β_4 and RIM1 from western blots of sucrose gradient fractions. The normalized density of each protein is plotted as a function of the sucrose density fraction number. (**c**) Coimmunoprecipitation of RIM1 with the β_4 subunit. Immunoprecipitation (IP) using an antibody for β_4 and subsequent WB for RIM1 was carried out on heparin-purified samples. A preparation from lethargic mice was used as a negative control. (**d**) Sucrose gradient fractionation of neuronal VDCC complexes from lethargic mouse brains. (**e**) Coimmunoprecipitation of VDCC subunits with RIM1. The immunocomplexes were disrupted by GST-BADN or GST-RIM1$_{1079-1463}$. IP using anti-RIM1 antibody and subsequent western blotting for $Ca_v2.1$ or β_4 was carried out.

non-VDCC complex. Syntaxin, a VDCC-interacting protein[18–21], showed similar cosedimentation with RIM1. Immunoprecipitation analysis of heparin-purified samples confirmed that the cosedimentation of RIM1 is due to its specific interaction with VDCC subunits (**Fig. 2c**). Antibody specific for β_4 precipitated RIM1 from wild-type mice, but not from lethargic mice (which carry a mutated form of the gene *Cacnb4*), expressing truncated β_4 protein lacking the α_1-interacting region[32,33]. It is unlikely that the β_4 isoform exclusively mediates the RIM1-VDCC association in the brain, as wild-type and lethargic mice were indistinguishable in the sucrose gradient profile (**Fig. 2d**). We designed a dominant-negative suppressor β_{4b} fusion construct (beta-AID dominant negative, BADN) to dissociate the activity of β-binding proteins such as RIM1 from the functional VDCC complex (**Supplementary Fig. 3** online). As residues 49–410 of the entire 519-amino-acid β_{4b} sequence are required for RIM1 binding (**Fig. 1b**), BADN was designed from the 'full-length' β_{4b} to efficiently quench RIM1. BADN also carries the β-interacting AID region from $Ca_v2.1$ buried at the α_1-binding site[33]. Because the intermolecular association of BADN with VDCC α_1 is inhibited by the intramolecular occlusion of the α_1-binding site in BADN, overexpression of BADN should deprive native β subunits of RIM1 without affecting their association with α_1. *In vitro* binding and coimmunoprecipitation experiments showed that BADN could bind to RIM1, but not to the AID-containing I-II linker region of $Ca_v2.1$ (**Supplementary Fig. 3**). Notably, the native RIM1-β association in partially purified brain VDCCs was disrupted by an 8-h co-incubation with 100 nM GST fusion proteins for BADN or RIM1$_{1079-1463}$ (**Fig. 2e**). *In vitro* binding of β_4 to RIM1$_{1079-1463}$ rapidly decayed with the addition of excess BADN (200 nM), indicating that this disruption is attributable to displacement of binding partners in the native association (**Supplementary Fig. 3**). These results provide evidence for a physiological association between native RIM1 and P/Q-type VDCCs via the β subunit in brain.

RIM1 targets to VDCC via β subunits at the plasma membrane

In recombinant HEK293 cells, β_{4b} and RIM1 were concentrated at the plasma membrane when they were coexpressed with the P/Q-type $Ca_v2.1$ α_1 subunit, whereas they were diffusively colocalized throughout the intracellular area in the absence of $Ca_v2.1$ (**Fig. 3a** and **Supplementary Fig. 4** online). The ratio of the fluorescence intensity at the plasma membrane, PM, to that in the cytoplasm, CYT—F_{PM}/F_{CYT}—was 0.52 ± 0.07 and 0.48 ± 0.07 with $Ca_v2.1$ and 0.10 ± 0.02 and 0.08 ± 0.02 without $Ca_v2.1$ for β_{4b} and RIM1, respectively. RIM1 localization to the plasma membrane via a membrane-targeted β-binding domain[27] composed of CD8 and the $Ca_v2.1$ I-II linker was elicited only after β_{4b} expression (**Fig. 3b** and **Supplementary Fig. 4**). The F_{PM}/F_{CYT} ratio was 0.29 ± 0.03 and 0.27 ± 0.02 with β_{4b}, and 0.08 ± 0.01 and 0.08 ± 0.02 without β_{4b} for the $Ca_v2.1$ I-II linker and RIM1, respectively. Notably, both the $Ca_v2.1$-mediated plasma membrane colocalization of RIM1 and β_{4b}, and the β_{4b}-mediated colocalization of RIM1 and the $Ca_v2.1$ I-II linker, were disrupted by BADN. In the presence of BADN, F_{PM}/F_{CYT} was 0.56 ± 0.11 and 0.19 ± 0.04 for β_{4b} and RIM1, respectively; and F_{PM}/F_{CYT} was 0.33 ± 0.04 and 0.13 ± 0.04 for the $Ca_v2.1$ I-II linker and RIM1, respectively. Thus, the RIM1-β_{4b} interaction is likely to be essential for the assembly of RIM1 with VDCC at the plasma membrane.

In cultured hippocampal neurons, RIM1 and β_{4b} both accumulated near presynaptic termini, in parallel with $Ca_v2.1$ clustering. These events had a substantially later onset than synaptogenesis, as shown by the synapsin I clustering observed at 8 days *in vitro* (DIV, **Fig. 3c,d**). Quantitative imaging showed that overexpression of either BADN or the RIM1 C terminus, RIM1$_{1079-1463}$, impaired the $Ca_v2.1$ clustering in presynaptic varicosities (**Fig. 3e,f**). The coincident targeting of RIM1 and β_{4b}, as well as the blockade of $Ca_v2.1$ accumulation by quenching of RIM1 and βs, suggests that the RIM1-β interaction regulates the localization of VDCCs at the presynaptic membrane. Because RIM1

© 2007 Nature Publishing Group http://www.nature.com/natureneuroscience

interacts with multiple proteins (**Fig. 1a**), the RIM1 effect observed using BADN and $RIM1_{1079–1463}$ could also be attributed to the quenching of other RIM interactions at different subcellular locations. However, a recent immunostaining study showed that the staining intensities for $Ca_v2.2$ and RIM covary at a giant calyx-type synapse[34], consistent with the idea that they are both components of transmitter release sites.

RIM1-β interaction modulates inactivation of VDCCs

To elucidate the functional significance of direct RIM1-β_4 coupling, we characterized whole-cell Ba^{2+} currents through recombinant VDCCs expressed as $\alpha_1\alpha_2/\delta\beta$ complexes containing various neuronal α_1 subunits: N-type $Ca_v2.2$, P/Q-type $Ca_v2.1$, R-type $Ca_v2.3$ and L-type $Ca_v1.2$ channels in BHK cells. The most prominent RIM1 effect on VDCC currents was observed on inactivation parameters. Inactivation was markedly decelerated in N-, P/Q-, R- and L-type currents (**Fig. 4a,b**). The same set of VDCC types also showed a significant depolarizing shift in the voltage dependence of inactivation (**Fig. 4c,d**; see **Supplementary Table 1** for statistical significance). In P/Q-type currents (with β_{4b}), RIM1 shifted the half-inactivation potential ($V_{0.5}$) by +24.6 mV, eliciting an inactivation curve with a component that was susceptible to inactivation induced at high voltages ($V_{0.5}$ (vector) = –45.9 mV, $V_{0.5}$ (RIM1) = –21.3 mV) and a component that was non-inactivating. In N- and R-type currents, RIM1 provoked a switch in the major phase of biphasic inactivation curves from low voltage induced ($V_{0.5}$ and ratio: –64.5 mV and 0.91 for N, and –78.2 mV and 0.91 for R) to high voltage induced ($V_{0.5}$ and ratio: –20.8 mV and 0.61 for N, and –27.9 mV and 0.53 for R). The L-type inactivation curve remained monophasic; however, the non-inactivating component was significantly augmented by RIM1 (from 0.07 to 0.25; $P < 0.05$). In P/Q-type, similar RIM1 effects on inactivation were observed with all other β subunits tested (**Fig. 4a,c** and **Supplementary Table 2** online). Furthermore, the C-terminal truncated mutants $RIM1_{1079–1463}$ and $RIM1_{1258–1463}$, but not $RIM1_{1079–1257}$, successfully slowed P/Q-type

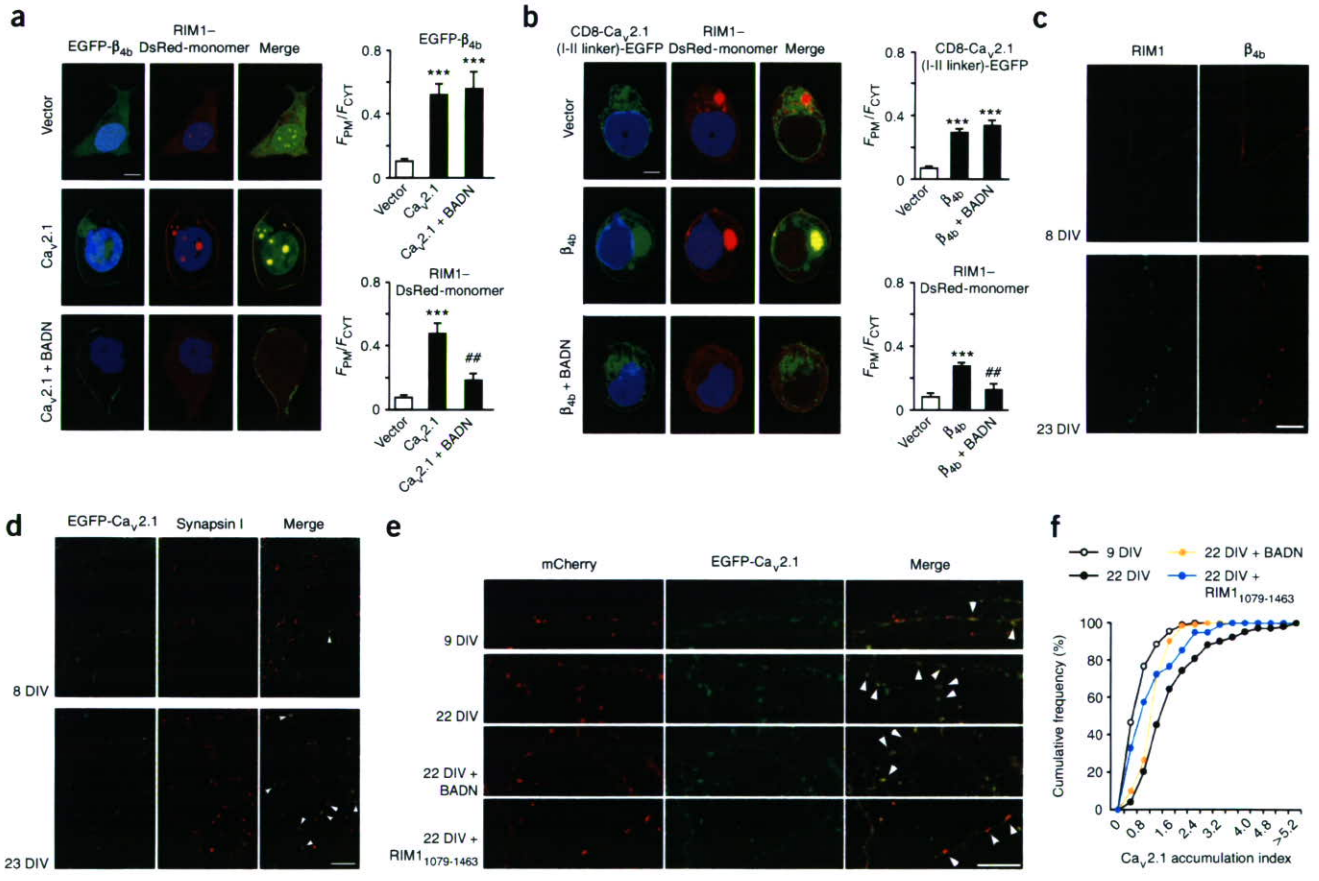

Figure 3 RIM1 clusters with the VDCC subunits near presynaptic termini in cultured hippocampal neurons. (**a**) $Ca_v2.1$ elicited plasma membrane (PM) colocalization of β_{4b} with RIM1. BADN disrupted colocalization. Left, confocal imaging of HEK293 cells expressing EGFP-β_{4b} and RIM1–DsRed-monomer with vector, $Ca_v2.1$ or $Ca_v2.1$ plus BADN. Scale bar, 5 μm. Nuclei were stained with Hoechst 33342. Right, subcellular location of EGFP-β_{4b} or RIM1–DsRed-monomer in 1-μm widths of the plasma membrane region and in the cytosolic area (CYT) ($n = 5$). $^{***}P < 0.001$ versus vector. $^{\#\#}P < 0.01$ versus $Ca_v2.1$. (**b**) β_{4b} elicited plasma membrane colocalization of $Ca_v2.1$(I-II linker) and RIM1. BADN disrupted colocalization. Left, confocal imaging of HEK293 cells expressing CD8-$Ca_v2.1$(I-II linker)-EGFP and RIM1–DsRed-monomer with vector, β_{4b} or β_{4b} and BADN. Right, subcellular location of CD8-$Ca_v2.1$(I-II linker)-EGFP or RIM1–DsRed-monomer ($n = 5$). $^{***}P < 0.001$ versus vector. $^{\#\#}P < 0.01$ versus β_{4b}. (**c**) Immunolocalization of tagged RIM1 and β_{4b} in cultured hippocampal neurons. Clustering of RIM1 and β_{4b} was undetected at 8 DIV, but was present at a substantially later stage at 23 DIV. Scale bar, 10 μm. (**d**) Late clustering of EGFP-$Ca_v2.1$ (arrowheads) in hippocampal neurons. Synapsin I–positive puncta were already abundant at 8 DIV, while $Ca_v2.1$ distribution was still diffuse. Like RIM1 and β_{4b}, $Ca_v2.1$ clustered much later on. (**e**,**f**) Accumulation of EGFP-$Ca_v2.1$ (arrowheads) in presynaptic varicosities was achieved between 9 and 22 DIV. This maturation process was impaired by $RIM1_{1079–1463}$ or BADN, suggesting that the local VDCC concentration at presynaptic active zones is influenced by RIM1–β-subunit interaction during a postsynaptogenic maturation period.

© 2007 Nature Publishing Group http://www.nature.com/natureneuroscience

(with β_{1a}) current inactivation (**Fig. 4a,c** and **Supplementary Table 3** online).

After RIM1 coexpression, single-channel P/Q-type currents clearly showed a prolongation of the mean time between first channel opening and last closing within a trace during 750-ms depolarizations to +20 mV without substantial changes in amplitude (0.59 pA, **Fig. 4e**). This observation corresponds well with the whole-cell data and suggests that RIM1 predominantly stabilizes the non-inactivating

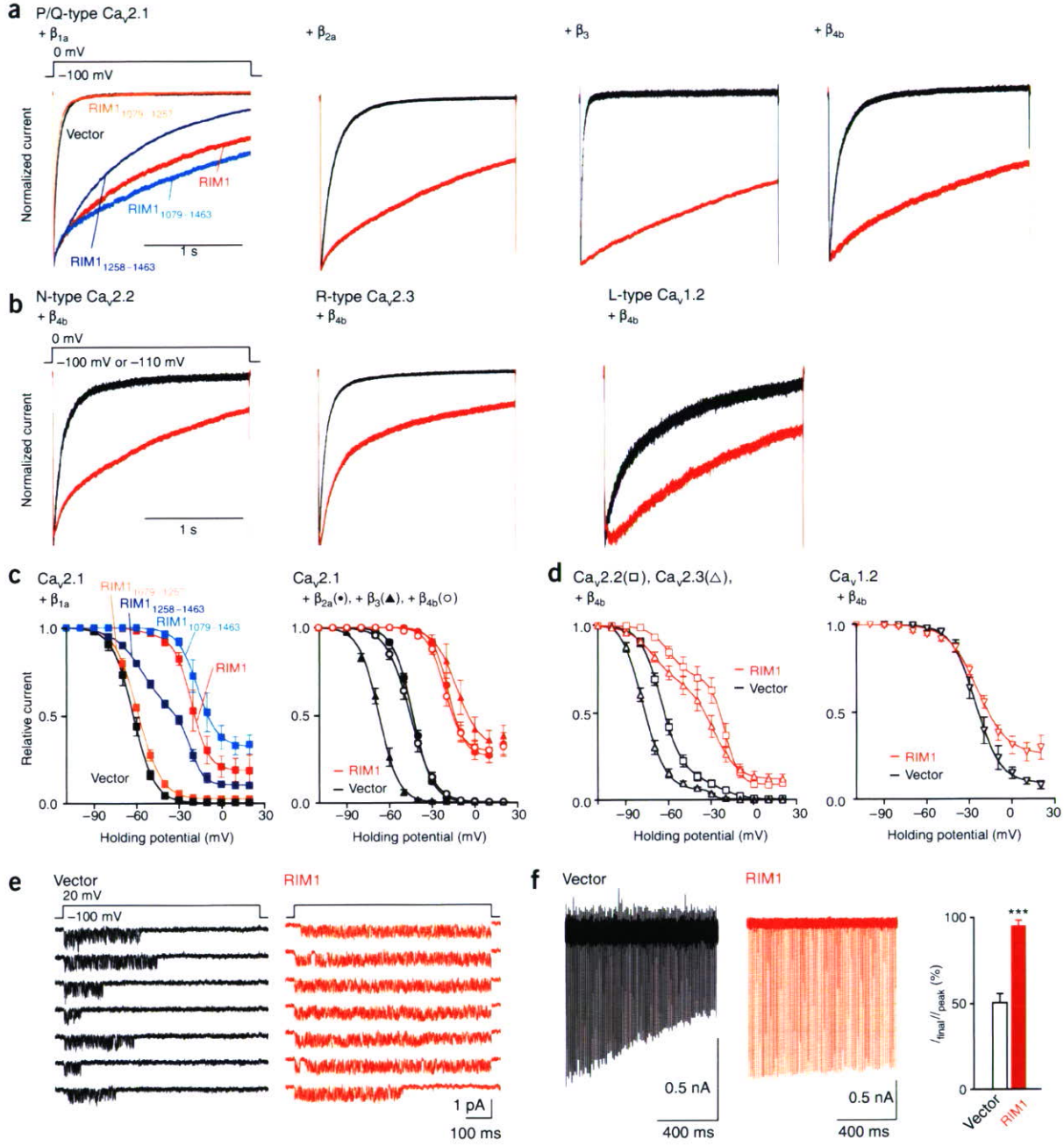

Figure 4 Effects of RIM1 on the inactivation properties of recombinant neuronal VDCCs. (**a**) Inactivation of P/Q-type $Ca_v2.1$ currents in BHK cells. The peak amplitudes before and after coexpression of RIM1 constructs were normalized for Ba^{2+} currents elicited by 2-s pulses to 0 mV from a holding potential (V_h) of −100 mV. (**b**) Inactivation of N-type $Ca_v2.2$, R-type $Ca_v2.3$ or L-type $Ca_v1.2$ currents (with β_{4b}). The V_h was −100 mV ($Ca_v2.2$, $Ca_v1.2$) or −110 mV ($Ca_v2.3$). (**c**) Left, inactivation curves for $Ca_v2.1$ (with β_{1a}). Right, inactivation curves for $Ca_v2.1$ in BHK cells expressing α_2/δ and different β subunits. See **Supplementary Tables 2** and **3** for statistical significance of the differences. (**d**) Inactivation curves for $Ca_v2.2$, $Ca_v2.3$ (left), or $Ca_v1.2$ (right) (with β_{4b}). See **Supplementary Table 1** for statistical significance of the differences. (**e**) RIM1 prolonged the time between first channel opening and last closing within a single-channel trace of $Ca_v2.1$ (with β_{4b}). Seven consecutive unitary traces are shown. The mean values for the time of each trace were 184.2 ± 33.3 ms ($n = 117$ traces) for vector and 502.8 ± 33.3 ms ($n = 101$) for RIM1. The time for traces without opening was counted as 0 ms. (**f**) Left, $Ca_v2.1$ currents (with β_{1a}) induced by 100-Hz action potential trains for 1 s. Right, percentage of currents in response to the last stimulus compared with the peak current ($n = 6$ for vector and $n = 4$ for RIM1). $^{***}P < 0.001$.

© 2007 Nature Publishing Group http://www.nature.com/natureneuroscience

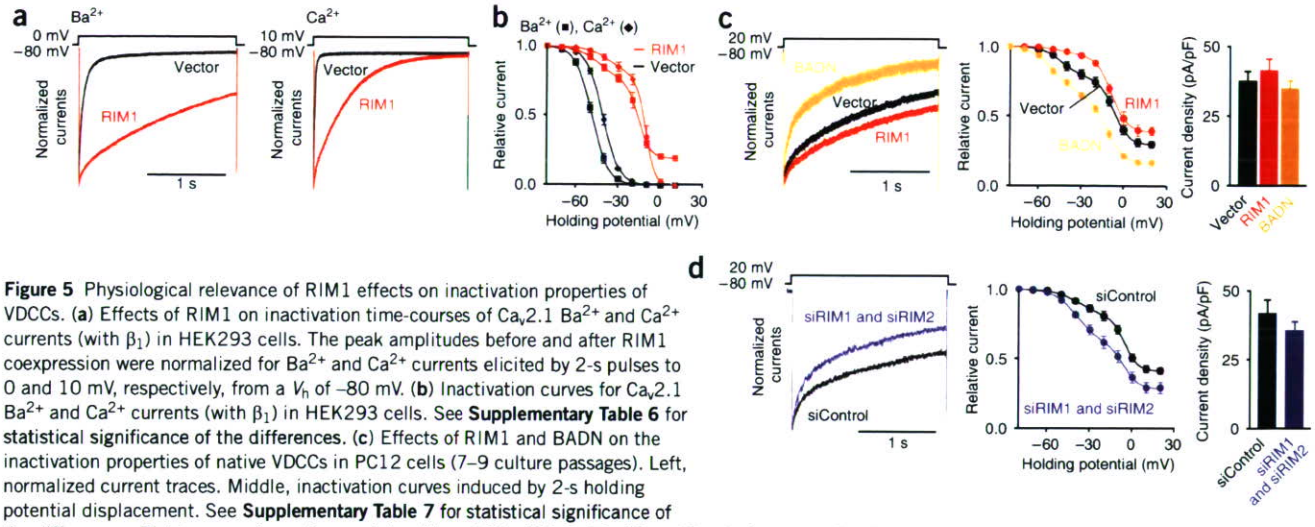

Figure 5 Physiological relevance of RIM1 effects on inactivation properties of VDCCs. (**a**) Effects of RIM1 on inactivation time-courses of $Ca_v2.1$ Ba^{2+} and Ca^{2+} currents (with β_1) in HEK293 cells. The peak amplitudes before and after RIM1 coexpression were normalized for Ba^{2+} and Ca^{2+} currents elicited by 2-s pulses to 0 and 10 mV, respectively, from a V_h of −80 mV. (**b**) Inactivation curves for $Ca_v2.1$ Ba^{2+} and Ca^{2+} currents (with β_1) in HEK293 cells. See **Supplementary Table 6** for statistical significance of the differences. (**c**) Effects of RIM1 and BADN on the inactivation properties of native VDCCs in PC12 cells (7–9 culture passages). Left, normalized current traces. Middle, inactivation curves induced by 2-s holding potential displacement. See **Supplementary Table 7** for statistical significance of the differences. Right, comparison of current densities at 10 mV ($n = 18$, 15 and 9 cells for vector, RIM1 and BADN, respectively). (**d**) Acceleration of inactivation by application of siRNAs specific for RIM1 and RIM2 (siRIM1 and siRIM2) in VDCC currents recorded from PC12 cells (2–3 culture passages). Left, normalized current traces. Middle, inactivation curves. See **Supplementary Table 7** for statistical significance of the differences. Right, comparison of current densities at 10 mV ($n = 6$ and 8 cells, for siControl, and siRIM1 and siRIM2, respectively).

mode[35]. Currents evoked by trains of action potential waveforms, a more physiological voltage-clamp protocol used to determine closed-state inactivation[36], further support the existence of a profound suppression of voltage-dependent inactivation by RIM1 (**Fig. 4f**).

The observed effect of RIM1 on VDCC inactivation is attributable to its association with the β subunit, as replacement of β_4 with the C-terminal truncation construct β_4-GK[37], which directly interacts with α_1 but lacks the ability to bind RIM1, did not substantially affect inactivation of N-type currents (**Supplementary Fig. 5** and **Supplementary Table 4** online). In addition, BADN significantly diminished the RIM1 effect on P/Q channel inactivation (**Supplementary Fig. 5** and **Supplementary Table 5** online for statistical significance). When 5 mM Ca^{2+} was used as a physiological charge carrier capable of inducing both Ca^{2+}-dependent and voltage-dependent inactivation[38], RIM1 still exerted prominent suppressive effects on inactivation in P/Q-type currents expressed in HEK293 cells (**Fig. 5a,b** and **Supplementary Table 6** online). Notably, in rat PC12 neuroendocrine cells, BADN or application of siRNAs that specifically suppress RIM1 and RIM2 expression accelerated inactivation and shifted the inactivation curve toward the hyperpolarizing direction (**Fig. 5c,d** and **Supplementary Table 7** online). This supports a physiologically significant role for RIM-mediated VDCC modulation via the β subunit. Notably, as observed in RIM1-expressing cells, voltage-dependent inactivation of presynaptic VDCC currents at membrane potentials ≥−40 mV has been previously demonstrated[39]. Thus, RIM1 exerts strong suppressive effects on the kinetics and voltage dependence of inactivation of VDCC currents.

RIM1's effects on other functional current parameters such as voltage dependence of activation, activation kinetics and current densities at different voltages in current-voltage relationships differentiate VDCCs into two different groups (**Fig. 6** and **Supplementary Table 1**). In β_{4b}-expressing BHK cells, the current densities of N- and P/Q-type currents were significantly augmented by RIM1, whereas those of R- and L-type currents were unaffected by RIM1 (**Fig. 6c,d**; and see **Supplementary Table 1** for statistical significance). In P/Q-type, $RIM1_{1079–1463}$, which binds β, was sufficient to enhance current density (**Fig. 6c**). By contrast, activation speeds were significantly reduced and activation curves were shifted toward positive potentials by RIM1 in R- and L-types, but not in N- and P/Q-types (**Fig. 6a,b**; and see **Supplementary Table 1** for statistical significance). Replacement of β_{4b} with other β isoforms abolished the augmentation of P/Q-type current densities by RIM1 (**Supplementary Fig. 6** online), but slowed the activation speed of P/Q-type by RIM1 (**Fig. 6b**). The RIM1 positive shift in activation curve was also elicited by β_{2a} in P/Q-type (**Supplementary Fig. 6**). Thus, N- and P/Q-type currents responded differently to RIM1 in terms of activation parameters and current densities than did R- and L-type currents, perhaps reflecting different subcellular localizations or functions of these channel subsets.

RIM1-β binding anchors neurotransmitter vesicles to VDCCs

We directly observed vesicles docked to the plasma membrane using evanescent wave microscopy, which illuminates only the subcellular area from the surface to a depth of less than 100 nm by total internal reflection fluorescence (TIRF). Dense-core vesicles were identified by a fusion protein of neuropeptide Y (NPY) and the fluorescent protein Venus in PC12 cells. The overlapping distribution of NPY-Venus, VAMP–DsRed-monomer and RIM1–DsRed-monomer indicated that transmitter-filled synaptic vesicles can be identified using the fluorescent signals of NPY-Venus (**Fig. 7a**). The codistribution is likely to be specific for RIM1, as caveolin-1–enhanced green fluorescent protein (EGFP) did not colocalize with VAMP–DsRed-monomer. The number of docked vesicles was increased significantly by expression of the full-length RIM1 ($P < 0.001$), whereas it was unaffected by $RIM1_{400–1078}$ or by $RIM1_{11–399}$, which forms a ternary complex with Rab3 and Munc13 via a Zn^{2+} finger critical for neurotransmitter release[40] (**Fig. 7b,c**). BADN, as well as $RIM1_{1079–1463}$, significantly attenuated the number of docked vesicles ($P < 0.001$ for BADN, $P < 0.05$ for $RIM1_{1079–1463}$). These inhibitory effects of BADN and $RIM1_{1079–1463}$ on vesicle docking most likely occur by quenching endogenous full-length RIMs and by saturating RIM1 interaction sites on VDCC β subunits, respectively. The BADN effect is not due to a reduction in the densities of VDCCs in PC12 cells, as BADN did not substantially affect current densities (**Fig. 5c**). Thus, the 'full-length' structure is probably essential for RIM1 to anchor neurotransmitter vesicles to VDCCs.

© 2007 Nature Publishing Group http://www.nature.com/natureneuroscience

© 2007 Nature Publishing Group http://www.nature.com/natureneuroscience

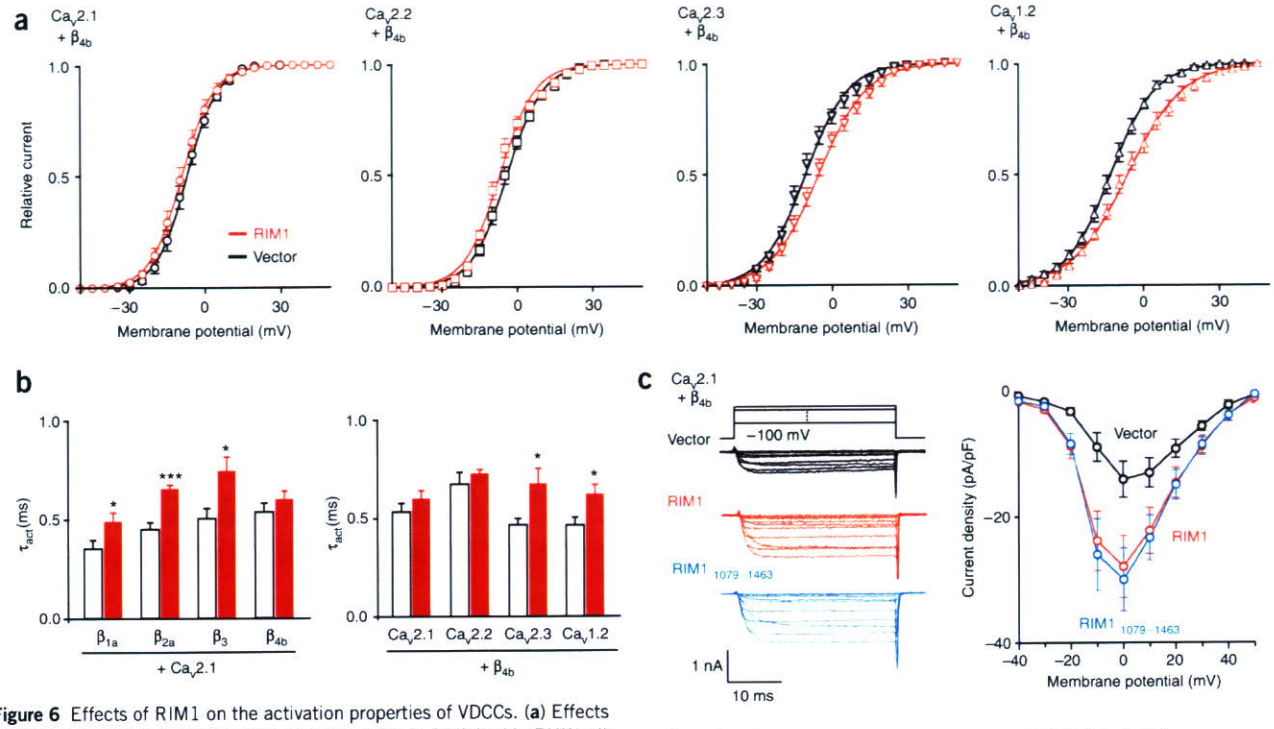

Figure 6 Effects of RIM1 on the activation properties of VDCCs. (**a**) Effects of RIM1 on activation curves of Ca_v currents (with β_{4b}) elicited in BHK cells. Tail currents elicited by repolarization to −60 mV after 5-ms test pulse from −50 to 50 mV were used to determine activation curves. See **Supplementary Table 1** for statistical significance of the differences. (**b**) Left, effects on activation speed of $Ca_v2.1$ channels containing various β subunits. Time constants were obtained by fitting the activation phase of currents elicited by 5-ms test pulse to 20 mV with a single exponential function. Right, effects of RIM1 on activation speed of Ca_v currents at 20 mV in various VDCC types. $^*P < 0.05$ and $^{***}P < 0.001$. (**c**) Effects of RIM1 proteins on P/Q-type $Ca_v2.1$. Left, representative traces for Ba^{2+} currents (with β_{4b}) on application of test pluses from −40 mV to 50 mV with 10-mV increments. Right, current density-voltage (*I-V*) relationships of $Ca_v2.1$. The V_h is −100 mV. See **Supplementary Table 2** for statistical significance of the differences. (**d**) *I-V* relationships of $Ca_v2.2$ (left) and $Ca_v2.3$ or $Ca_v1.2$ (right) (with β_{4b}). The V_h is −100 mV ($Ca_v2.2$, $Ca_v1.2$) or −110 mV ($Ca_v2.3$). See **Supplementary Table 1** for statistical significance of the differences.

RIM1-β interaction enhances neurotransmitter release

We studied the physiological relevance of RIM1 interactions with the VDCC complex by assessing neurotransmitter release from PC12 cells in which diverse high voltage–activated VDCC types have been precisely characterized[35,41] (**Supplementary Fig. 7** online). We transfected PC12 cells with RIM1 construct cDNAs along with *Chat* (encoding choline acetyltransferase), which synthesizes acetylcholine (ACh) for synaptic vesicles[42]. ACh release, triggered by Ca^{2+} influx in response to high-K^+ (elevation of extracellular K^+ concentration from 5.9 mM to 51.1 mM) membrane depolarization, was significantly potentiated by full-length RIM1 (**Fig. 8a** and **Supplementary Fig. 7**, $P < 0.001$). ACh release was also enhanced by the Rab3-interacting N-terminal $RIM1_{11–399}$ and by the C-terminal $RIM1_{1079–1463}$ that maintains VDCC currents, but not by the middle $RIM1_{400–1078}$. In contrast, BADN significantly suppressed ACh release ($P < 0.001$). In cultured cerebellar neurons, similar suppression by BADN and potentiation by the full-length RIM1 were observed for high K^+–induced glutamate release (**Fig. 8b**). The results suggest that RIM1 potentiates neurotransmitter release through its interaction with VDCC β in neuronal and neuron-like cells.

DISCUSSION

The present investigation reveals a previously unknown physical association between the presynaptic active zone proteins RIM1 and VDCC β subunits. The results of yeast two-hybrid assays, *in vitro* binding assays and coimmunoprecipitation experiments have identified a RIM1-VDCC complex formed by direct interaction of the β subunit with the α_1 subunit AID region and the RIM C terminus (residues 1079–1463) (**Fig. 1**). The identification of native RIM1-VDCC complexes in brain (**Fig. 2**), the colocalization of RIM1 with VDCC subunits at the plasma membrane and the presynapse, and the disruption of such localization and complex formation by BADN (**Fig. 3**) support a physiological role for the RIM1-β association. Further biochemical and functional analyses (**Figs. 1** and **4**) suggest that $RIM1_{1079–1257}$ and $RIM1_{1258–1463}$ are the primary β subunit binding site and modulatory region, respectively, in the RIM1 protein. Although our experiments showed that RIM1 and β_4 interacted, the RIM1 in wild-type brains was indistinguishable from that found in the brains of lethargic mice by sucrose gradient profile (**Fig. 2a,d**). It has been previously reported that the immunolocalization of $Ca_v2.1$ and $Ca_v2.2$ in the brain and the properties of P-type currents in Purkinje